TECHNICAL ARTICLE

Effect of Annealing on Microstructure Evolution and Tensile Behavior of Hot-Rolled FeMnCoCrAl High-Entropy Alloy

Fuben Chu, Zhengyou Tang, Zeyu You, and Li Zhao

In this study, a new composition of HEA $((Fe_{50}Mn_{30}Co_{10}Cr_{10})_{91}Al_9$, at.%) was designed, and the microstructure evolution and tensile behavior of hot-rolled $(Fe_{50}Mn_{30}Co_{10}Cr_{10})_{91}Al_9$ (at.%) high-entropy alloy (HEA) were investigated after annealing at various temperatures. The HEA exhibited a three-phase structure of the FCC phase, BCC phase, and a small amount of HCP phase after hot rolling and annealing. Annealing at lower temperatures led to a higher fraction of BCC phase and sub-crystalline grains in the recovery state, making the HEA have high strength. After annealing at high temperatures, the fraction of FCC phase increased. The fraction of recrystallized grains and twin boundaries in the HEA also increased, improving the ductility of the HEA. The HEA exhibited a multistage strain-hardening mechanism during deformation, which was rarely seen in traditional HEAs. The relationship between the microstructure and mechanical properties was discussed from the lattice frictional stress, solid solution strengthening, phase fractions, grain sizes, and dislocation.

1. Introduction

The emergence of high-entropy alloys (HEAs) has broken traditional alloy design ideas and provided a new direction for developing metal materials (Ref 1-4). Because of their high mixing entropy, high-entropy alloys tend to form disordered solid solution structures, such as face-centered cubic (FCC) (Ref 5), body-centered cubic (BCC) (Ref 6), and hexagonal close-packed (HCP) (Ref 7) structures. Early research focused on HEAs with single-phase structures, such as CoCrFeMnNi (Ref 4) high-entropy alloys with single-phase FCC structures and CoCrFeNiAl (Ref 8) high-entropy alloys with single-phase BCC structures. These single-phase alloys exhibit superior performance in terms of strength or ductility but cannot achieve a trade-off between strength and ductility (Ref 9). To overcome the deficiency of strength or ductility of high-entropy alloys with single-phase structures, HEAs composed of FCC and BCC phases have been developed to improve their performance. (Ref 10-12). To date, many dual-phase high-entropy alloys have been developed, and Al-containing dual-phase high-entropy alloys are the most studied. Al is one of the most common

components in high-entropy alloys, and adding Al can promote the formation of the BCC phase. He et al. (Ref 13) studied the effect of Al addition on the structural evolution and tensile properties of CoCrFeNiMn. When the content of Al is less than 8% (atomic fraction), the alloy is a single-phase FCC solid solution. When the content of Al is between 8 and 16%, the alloy is FCC plus BCC dual-phase; when the Al content is higher than 16%, the alloy is single-phase BCC. In 2016, Li et al. (Ref 14) proposed the strategy of metastable engineering. They prepared a dual-phase $Fe_{50}Mn_{30}Co_{10}Cr_{10}$ high-entropy alloy with the TRIP effect, which has decent tensile strength and ductility. However, its yield strength is low, so it easily fails when applying an external stress. Both single-phase and dual-phase high-entropy alloys have some shortcomings in terms of performance. Undoubtedly, developing tri-phase high-entropy alloys based on dual-phase high-entropy alloys will be a new direction in the research of high-entropy alloys.

For HEAs, annealing is a pivotal step to improve the microstructure and mechanical properties. Heterogeneous microstructures with various grain sizes can be obtained by annealing, thus obtaining an excellent strength-ductility combination. The C-doped FeNiMnAlCr high-entropy alloy prepared by Wu et al. (Ref 15) obtained a combination of ultimate tensile strength of 765 MPa and elongation of 32.6% after hot rolling and annealing. Its yield strength increased by 168 MPa compared to the as-cast alloy. Most of the previous research focuses on improving the performance of high-entropy alloys through annealing. However, there are few studies on the effects of annealing on the microstructure and mechanical behavior of HEAs. HEAs with multiphase structures are often accompanied by complex solid-state phase transformations during annealing. Therefore, more research is still needed to study the effect of annealing on the microstructure evolution and tensile behavior of HEAs and to reveal the relationship between the microstructure and mechanical properties.

Fuben Chu, Zeyu You, and Li Zhao, School of Materials Science and Engineering, Northeastern University, Shenyang 110819, China; and Zhengyou Tang, School of Materials Science and Engineering, Northeastern University, Shenyang 110819, China; and Key Laboratory of Lightweight Structural Materials, Northeastern University, Shenyang 110819, China. Contact e-mails: sdkjdxcfb@163.com and tangzy@smm.neu.edu.cn.

In this study, $(Fe_{50}Mn_{30}Co_{10}Cr_{10})_{91}Al_9$ (at.%) HEA consisting of a tri-phase structure was prepared. The effects of different annealing temperatures after hot rolling on the microstructure evolution and tensile behavior of the alloy were studied. In addition, the relationship between the microstructure and mechanical properties was described using a simple composite model to discuss the effect of the annealing heat treatment in the present alloys. This study hopes to make some theoretical contributions to the further study of high-entropy alloys with tri-phase structures.

2. Materials and Methods

The HEA ingot with a nominal composition of $(Fe_{50}Mn_{30}Co_{10}Cr_{10})_{91}Al_9$ (at.%) was prepared in an arc melting furnace. The raw materials used in the present work were pure metals Fe, Mn, Co, Cr, and Al (purity > 99.95%). The ingot used in the present work was remelted at least four times to ensure chemical homogeneity. Then, the ingot was forged into a square billet with a section of 100×15 mm2, air-cooled to room temperature, subsequently hot-rolled at 1173 K with a reduction ratio of 87% (thickness reduced from 15 to 2 mm), and then cooled with water. These plates were subsequently annealed at 873, 973, 1073, and 1173 K for one hour in a vacuum environment.

The tensile test was carried out on a SANSCMT5000 universal electronic mechanical testing machine at room temperature according to ASTM E8/E8M. Dog bone-shaped samples with dimensions of 25 mm (gauge length) × 6 mm (width) × 2 mm (thickness) were uniaxially tensioned under a strain rate of 10^{-3} s^{-1}.

Phase identification of $(Fe_{50}Mn_{30}Co_{10}Cr_{10})_{91}Al_9$ (at.%) HEA was analyzed by x-ray diffraction (XRD) using a Smartlab Rigaku Corporation x-ray diffractometer with an incident beam of Cu Kα radiation. The scans were performed from 40 to 100° of 2θ with a step size of 0.02 and scan speed of 5°/min. The alloy microstructure was observed by electron backscattered diffraction (EBSD, Carl Zeiss AG, crossbeam 550, step size 80 nm) and scanning electron microscopy (SEM, SSX-550) with an energy-dispersive (EDS) detector. The EBSD data were analyzed by HKL channel 5 and ATEX software. The specimens were electropolished in a solution of perchloric acid alcohol.

3. Results

3.1 Phase and Microstructure Changes After Annealing

Figure 1 shows an XRD pattern of the samples after hot rolling and annealing. The samples were composed of FCC, BCC, and a small amount of HCP phase. A small amount of the HCP phase was formed during quenching after hot rolling and annealing. However, the content of the HCP phase in the annealed specimen is small and cannot be clearly observed in the XRD pattern. After annealing at 873 K, the peak value of the BCC phase was higher than that of the FCC phase. With increasing annealing temperature, the peak intensity ratio of I (111) FCC and I (110) BCC increased and reached a maximum at 1073 K. When the annealing temperature increased to 1173 K, the peak value of the FCC phase decreased.

Figure 2 shows the SEM-BSE micrograph of the specimens after hot rolling and annealing. Figure 2(a) shows the microstruc-
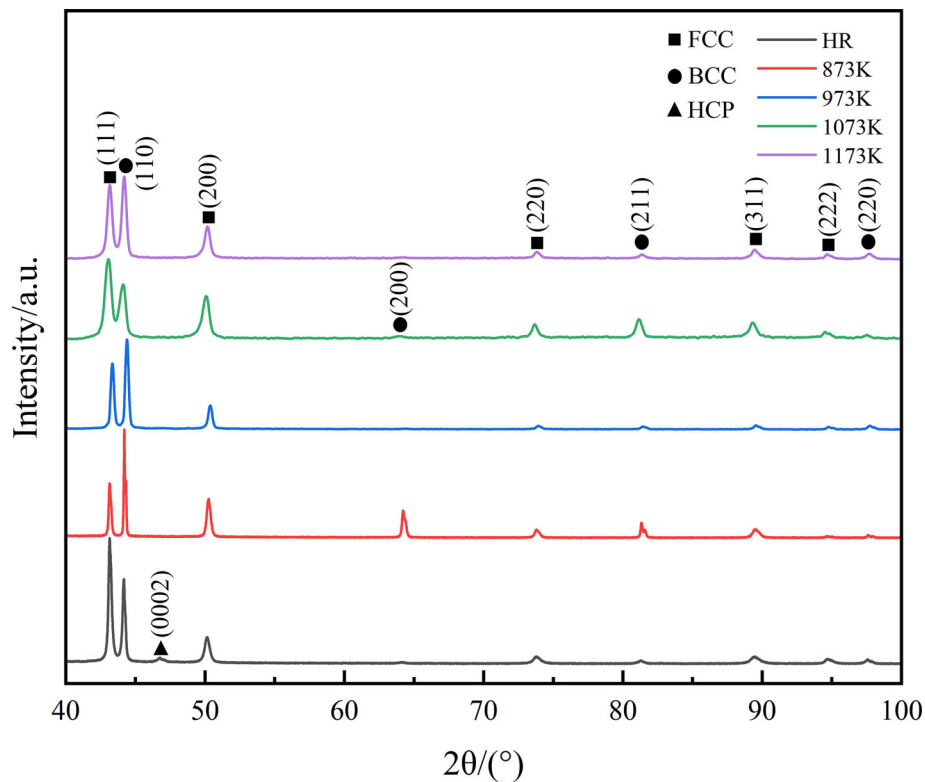

Fig. 1 XRD patterns of hot-rolled and annealed samples
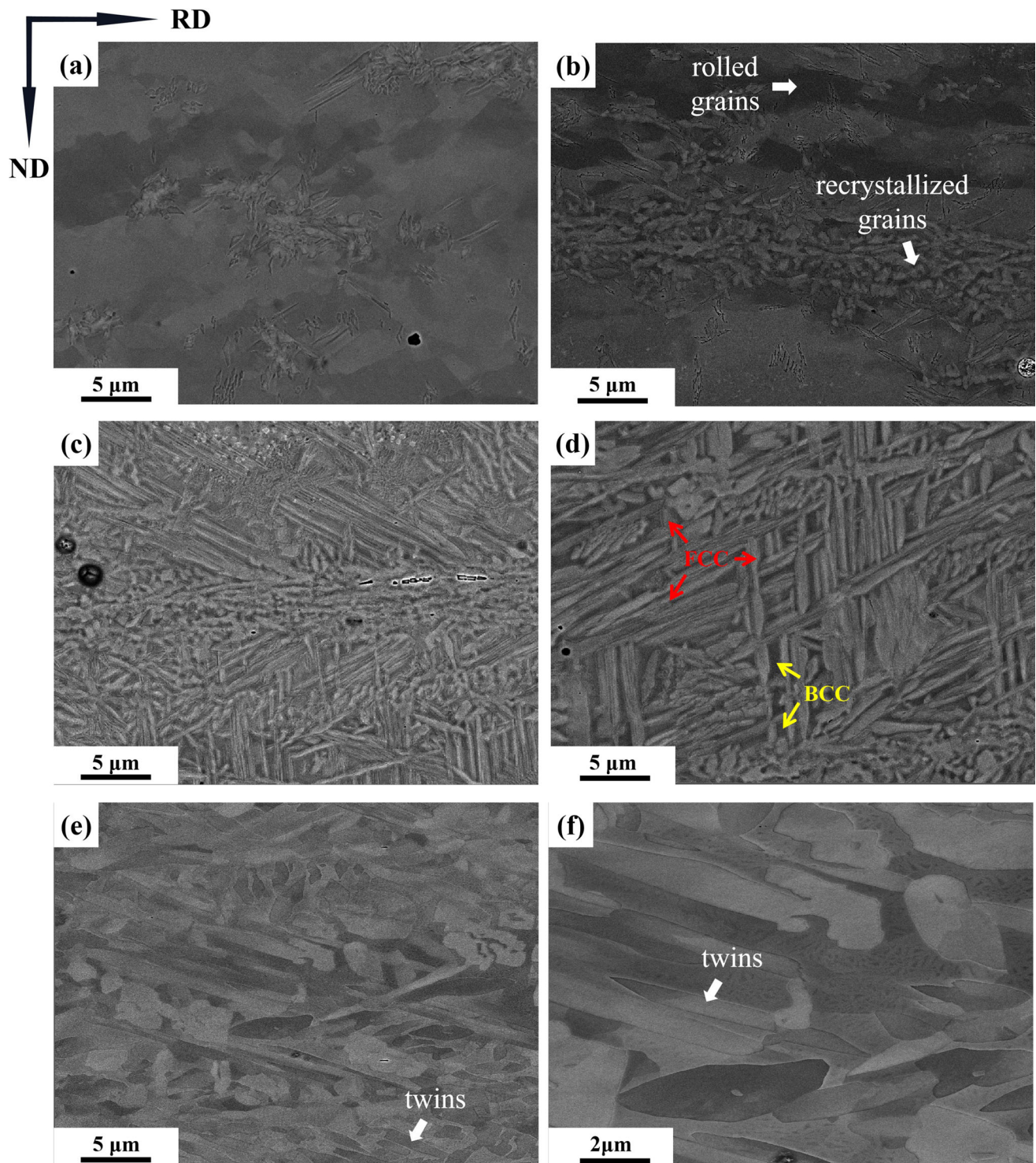
Fig. 2 Microstructure BSE images of cold-rolled and annealed samples: (a) hot-rolled, (b) 873 K-annealed, (c) 973 K-annealed, (d) 1073 K-annealed, (e)– (f) 1173 K-annealed

ture of the hot-rolled specimen. The hot-rolled specimen contained many rolled grains and a small number of recrystallized grains. After annealing at 873 K, there were still some rolled grains. However, the number of recrystallized grains was higher than that of the hot-rolled specimen. After annealing at 973 K-1073 K, the rolled grains entirely disappeared, and some recrystallized grains began to grow into columnar grains. Compared with the grains annealed at 973 K, the grain size after annealing at 1073 K was larger. As the annealing temperature increased to 1173 K, the grain coarsening was more severe, and some annealing twins were found. Many annealing twins in the alloy's microstructure may indicate that the alloy has a lower stacking fault energy (SFE) (Ref 16, 17). Another HEA with a low SFE (e.g., CoCrFeMnNi or CoCrFeNi HEA) has also been reported to have abundant annealing twins in recrystallized microstructures (Ref 18, 19).
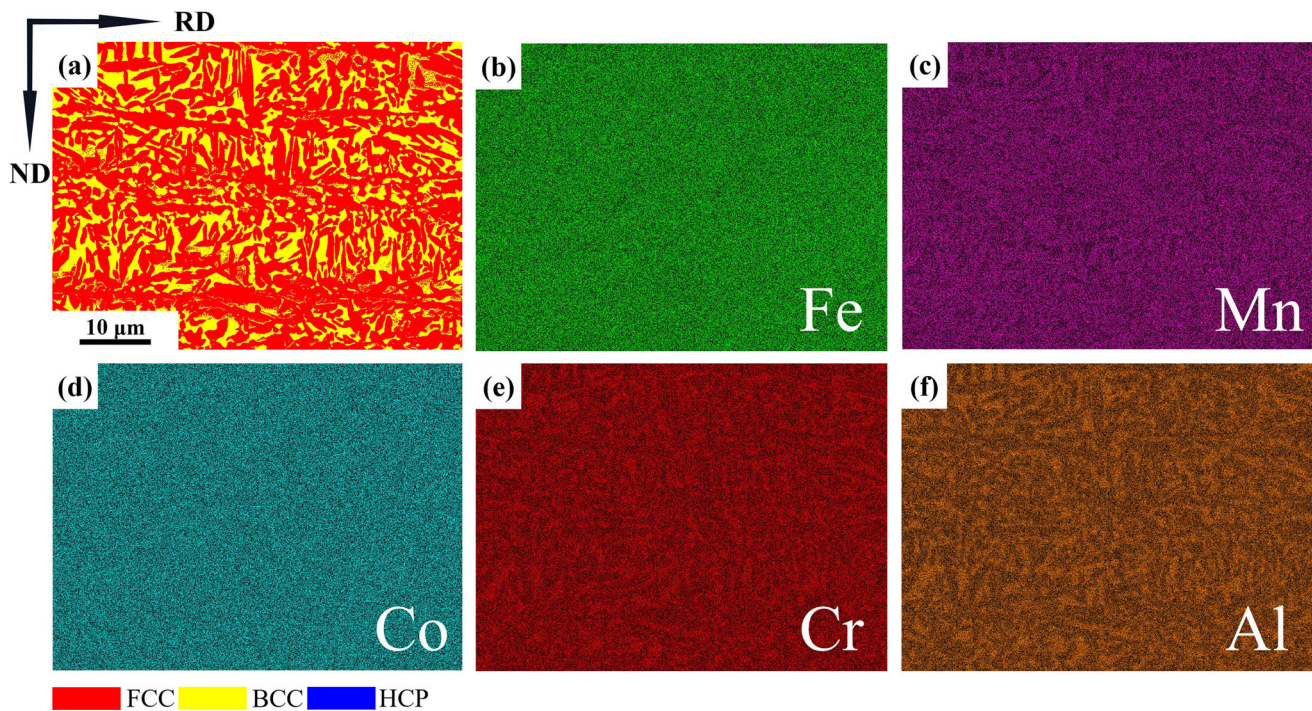
Fig. 3 EBSD images and EDS mapping results of the sample annealed at 1073 K: (a) phase map, (b-f) element distributions

**Table 1 EDS analysis results of the 1073 K annealed sample, at%**

Regions	Fe	Mn	Co	Cr	Al
FCC	45.07	30.57	10.01	8.38	5.97
BCC	43.85	24.72	9.32	12.02	10.09

Elemental distributions within alloys were characterized by EDS, as presented in Fig. 3 and Table 1. Fe and Co were uniformly distributed without segregation. Al and Cr were enriched in the BCC phase region, while Mn was enriched in the FCC phase region. It has been shown that Al usually acts as a stabilizer of the ordered BCC/B2 phase in biphasic HEA (Ref 20). Similar results have been widely reported for some HEAs containing Al (Ref 20-22).

To further explore the microstructure of the specimens after annealing, an EBSD analysis was carried out, as shown in Fig. 4. From Fig. 4(a), (b), (c) and (d), the microstructure of the annealed specimens showed completely different grain sizes and distribution characteristics. According to Fig. 4(e), (f), (g), (h), and (l), after annealing at 873 K, the proportion of sub-crystals in the restored state of the sample was as high as 85.8%, while the proportion of recrystallized grains was only 10.1%. The grain orientation in the FCC phase was random, while a strong preferred crystal orientation appeared in the BCC phase, which indicated that there were almost no recrystallized grains in the BCC phase, even at 873 K. As the annealing temperature increased to 973 K, the content of the FCC phase increased compared to that after annealing at 873 K, and the proportion of recrystallized grains increased to 15.2%. The specimens annealed at 1073-1173 K were mainly composed of grains with random orientation, and the proportion of recrystallized grains increased to 46.8% and 54.3%,

respectively. Compared with the traditional single-phase high-entropy alloy, many recrystallized grains were in the FCC phase in this study. In contrast, the content of recrystallized grains in the BCC phase was still very small, indicating that the recrystallization process of the BCC phase was still slow, even at 1173 K.

The distribution of grain boundaries in HEAs and the proportion of various grain boundaries can affect the properties of alloys (Ref 23). High-angle grain boundaries (HAGBs) are defined as having an orientation difference greater than or equal to 15 degrees, and low-angle grain boundaries (LAGBs) have an orientation difference between 2 and 15 degrees. Twin grain boundaries are defined as having an orientation difference close to 60 degrees (Ref 24). Figure 5 shows the proportion of various grain boundaries. After annealing at 873 K, the proportion of low-angle grain boundaries was 40.8%, and high-angle grain boundaries accounted for 59.2%. These data show that after annealing at 873 K, there were still many recovered subgrains in the specimen, even if partial recrystallization occurred. Under the joint action of heat energy and deformation energy, the homogenized grains in the hot-rolled specimen undergo severe plastic deformation and transform into subgrains. The subgrains store high deformation energy and high-density dislocations, which are thermodynamically unstable (Ref 25). After annealing at 873 K, only partial recrystallization occurred, and the deformation energy stored in the subgrains could not be entirely released. After annealing at 973-1073 K, the proportion of high-angle grain boundaries increased further. However, as mentioned above, the BCC phase cannot entirely recrystallize, and the proportion of low-angle grain boundaries was still high. After annealing at 1173 K, the proportion of high-angle grain boundaries and twin boundaries increased. The generation of twins was considered a form of releasing deformation energy in grains during recrystallization annealing, which can significantly reduce the
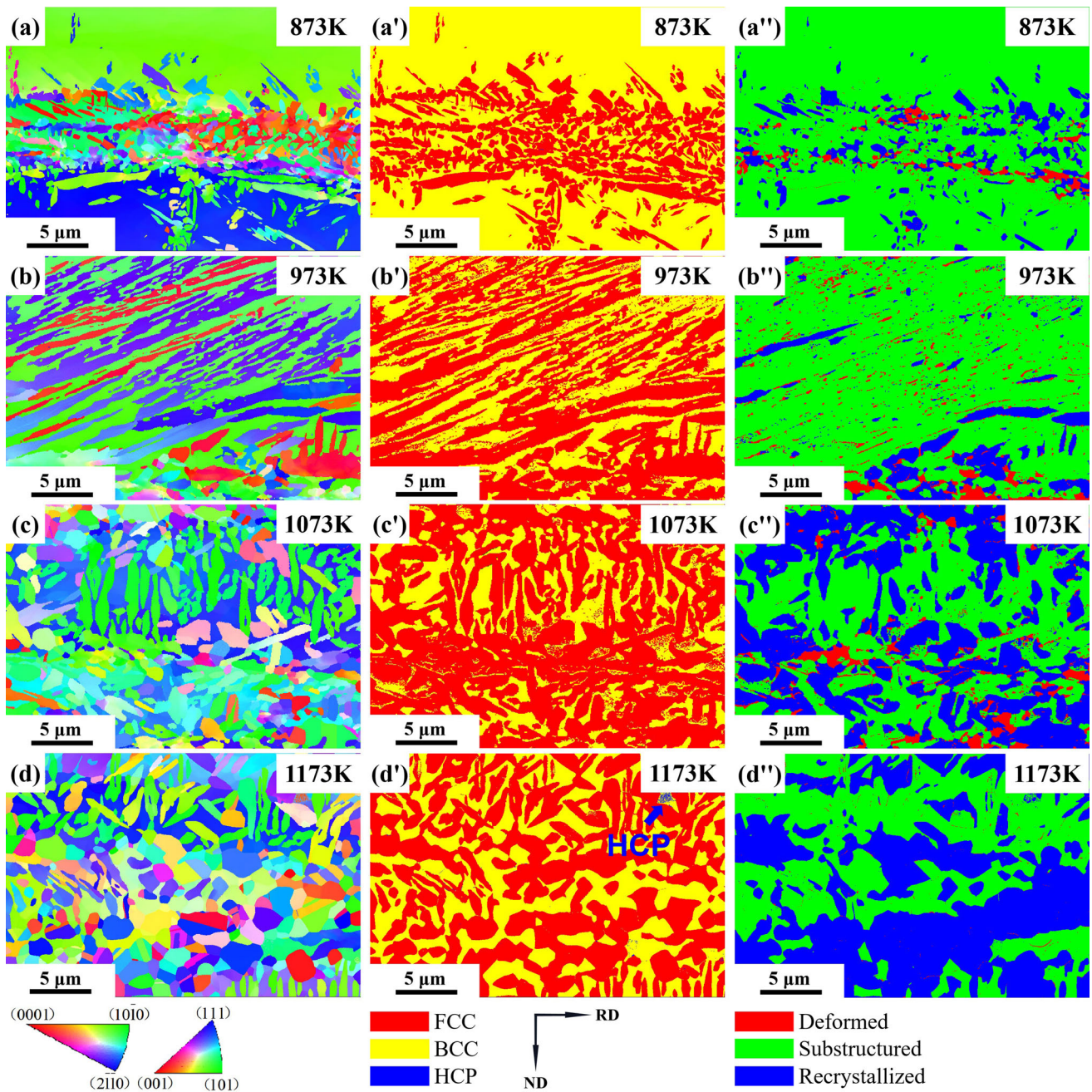
Fig. 4 EBSD images of samples annealed at different temperatures: (a-d) IPF maps, (a′-d′) phase maps, (a″-d″) deformed, substructured and recrystallized regions of annealed samples, (a-a″) 873 K-annealed, (b-b″) 973 K-annealed, (c–c″) 1073 K-annealed, (d-d″) 1173 K-annealed

dislocation density (Ref 26). In this study, the annealing temperature had an evident influence on the recrystallization of the HEA. With increasing annealing temperature, the proportion of high-angle grain boundaries and twin boundaries increased. However, even at 1173 K, the BCC phase had not entirely recrystallized. Whether the annealing temperature can increase the proportion of twins remains to be explored. However, it is worth noting that studies have shown that in some single-phase high-entropy alloys, increasing the annealing temperature will increase the proportion of twins (Ref 27). Nevertheless, when the annealing temperature is further increased, the ratio of twin grain boundaries will decrease. The recrystallized grains are transformed into typical polygonal grains (Ref 28).

3.2 Tensile Mechanical Properties of HEAs

Figure 6 shows the tensile properties of hot-rolled and annealed samples. Figure 6(a) shows the engineering stress–strain curves of hot-rolled and annealed samples. The average ultimate tensile strength (UTS), yield strength (YS), and elongation (EL) of the samples are shown in Fig. 6(b). The yield strength of the hot-rolled sample was 623.37 MPa, the ultimate tensile strength was 709.98 MPa, and the elongation rate was 13.64%. After annealing at 873 K, the yield strength of the sample increased to 713.67 MPa, the tensile strength increased to 893.11 MPa, and the elongation slightly improved to 14.60%. The sample annealed at 873 K had more recrystallized grains and BCC phase than the hot-rolled sample. The
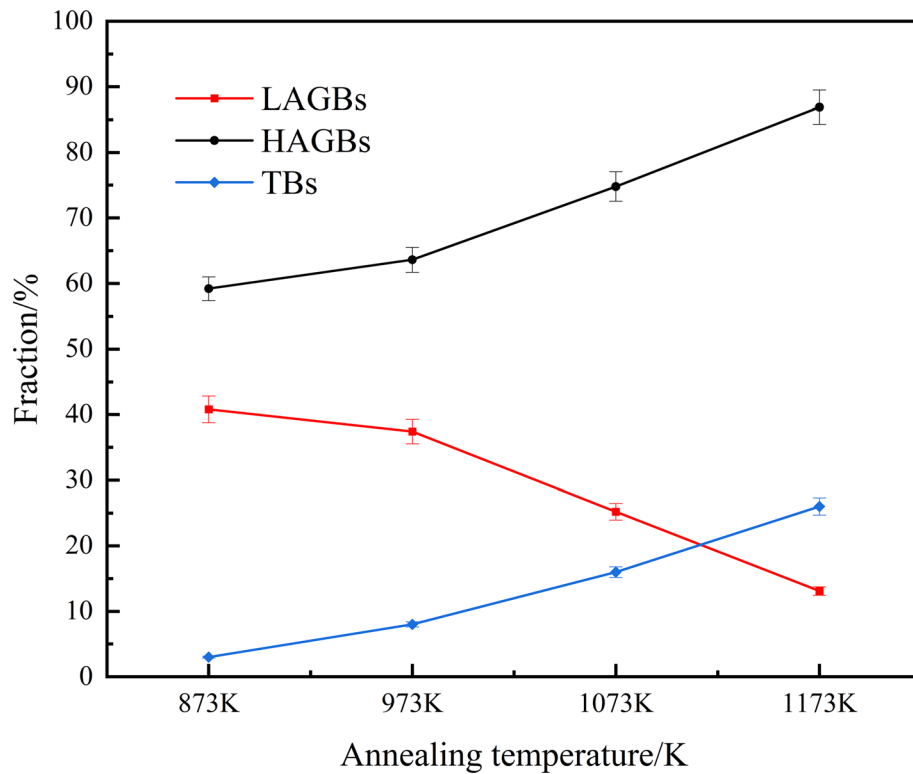
Fig. 5 Fractions of various grain boundaries of the samples annealed at different temperatures
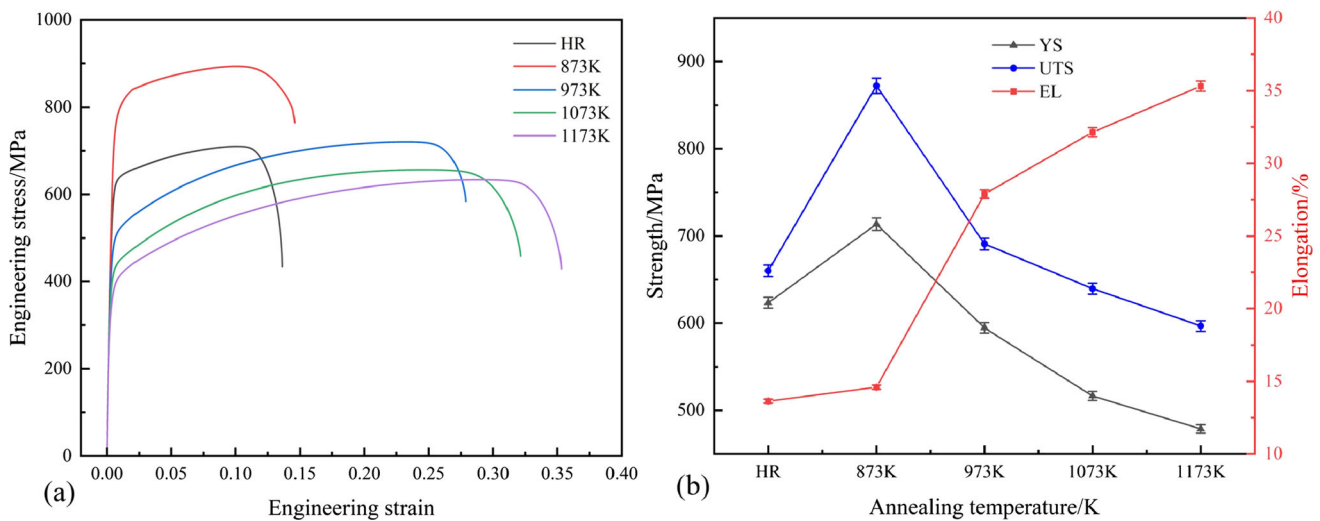
Fig. 6 Tensile properties of hot-rolled and annealed samples: (a) Engineering stress–strain curve, (b) yield strength, tensile strength and elongation

content of the BCC phase increased so that the strength increased. Moreover, the increased recrystallized grain content increases the ductility of the sample. As the annealing temperature increased to 973 K, the yield strength decreased from 713.67 MPa to 594.66 MPa, and the ultimate tensile strength decreased from 893.11 MPa to 720.78 MPa. However, the elongation increased significantly, from 14.6% to 27.88%. When the annealing temperature continued to increase, the strength continued to decrease, but the decrease was smaller than before. Correspondingly, the ductility increased.

In a series of AlFeMnCoCrNi high-entropy alloys with different Al content studied by He (Ref 13) et al., the BCC phase in the alloy increased with the increase in Al content significantly, making the alloy have a higher strength. In this study, annealing at a lower temperature promoted the formation of a hard BCC phase in a soft FCC matrix, which gave the sample higher strength after annealing at 873 K. However, increasing the hard phase proportion increased the alloy's strength, corresponding to the ductility loss of the sample. When the annealing temperature increased, the hard BCC phase
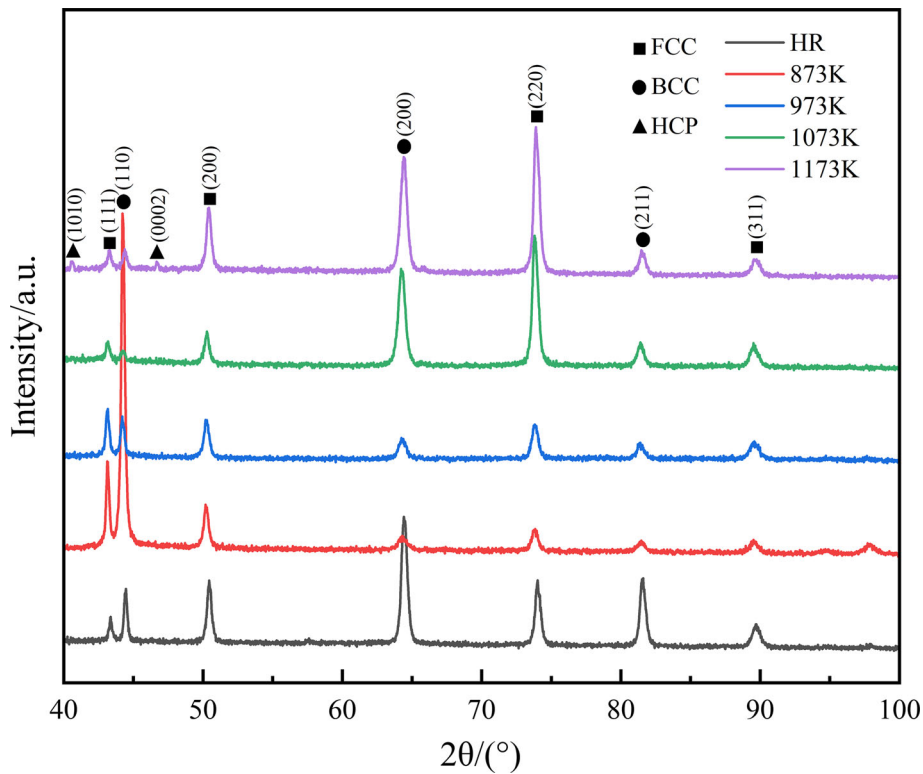
Fig. 7 XRD patterns of hot-rolled and annealed samples after tensile deformation

in the sample decreased, which made the strength of the sample begin to decrease, but the ductility increased.

3.3 Microstructure Evolution After Tensile Deformation

Figure 7 shows the XRD patterns of hot-rolled and annealed samples after deformation. A more pronounced three-phase structure appears in the deformed alloy, especially in the sample annealed at 1193 K. The intensity of the diffraction peaks of FCC decreased, and the peak of the BCC phase after deformation was stronger than that before deformation. However, in the sample annealed at 873 K, the peak strength of the BCC phase (110) is abnormally high, possibly because some grains with strong preference orientation are still retained.

Figure 8 shows EBSD images of samples annealed at different temperatures after tensile deformation. The BCC phase of the sample annealed at 873 K still retained a strong preferred orientation after tensile deformation. In contrast, the FCC phase elongated toward the tensile direction. At the same time, most of the grains in the samples annealed at 973-1173 K elongated along the tensile direction after tensile deformation.

Figure 9 shows the volume fraction of each phase in the samples before and after deformation. The content of the HCP phase and BCC phase increased after tensile deformation, and the content of the FCC phase after deformation was lower than that before deformation, which indicated that the TRIP effect occurred during plastic deformation. In the deformation process, a part of the FCC phase changed into the HCP phase with a hexagonal structure. However, this change was minimal. From the dynamic point of view, the difficulty of transforming the FCC structure into an HCP structure depends on the energy barrier at the γ-interface. The higher the energy barrier is, the more difficult it is to transform (Ref 29-31). In this study,

because of the addition of Al, the SFE of the alloy increased. The calculated SFE of the alloy was 34.51 mJ/m^2, but when SFE > 20 mJ/m^2, the γ → ε phase transformation will be inhibited. In addition, the addition of Al increases the types of atoms in the alloy, increases the potential energy fluctuation on the lattice, and enhances the interaction between atoms, which leads to the slow movement of atoms and increases the energy barrier, so it is not conducive to the transformation from the FCC phase to the HCP phase (Ref 30). However, with the increase in annealing temperature, the growth trend of the HCP phase was more significant. On the one hand, the energy of the FCC phase increased due to the increase in temperature, and the atoms moved more frequently, making breaking through the energy barrier easier. On the other hand, the FCC phase after high-temperature annealing was more abundant, and the HCP phase's nucleation position increased, leading to more metastable austenite transforming to the HCP phase.

4. Discussion

4.1 Strain-Hardening Behavior

The true stress and strain data can be calculated from the engineering stress and strain data obtained from the tensile test. Figure 10(a) shows the true stress–strain curve. Then, the following formula was used to calculate the strain-hardening rate of the samples:
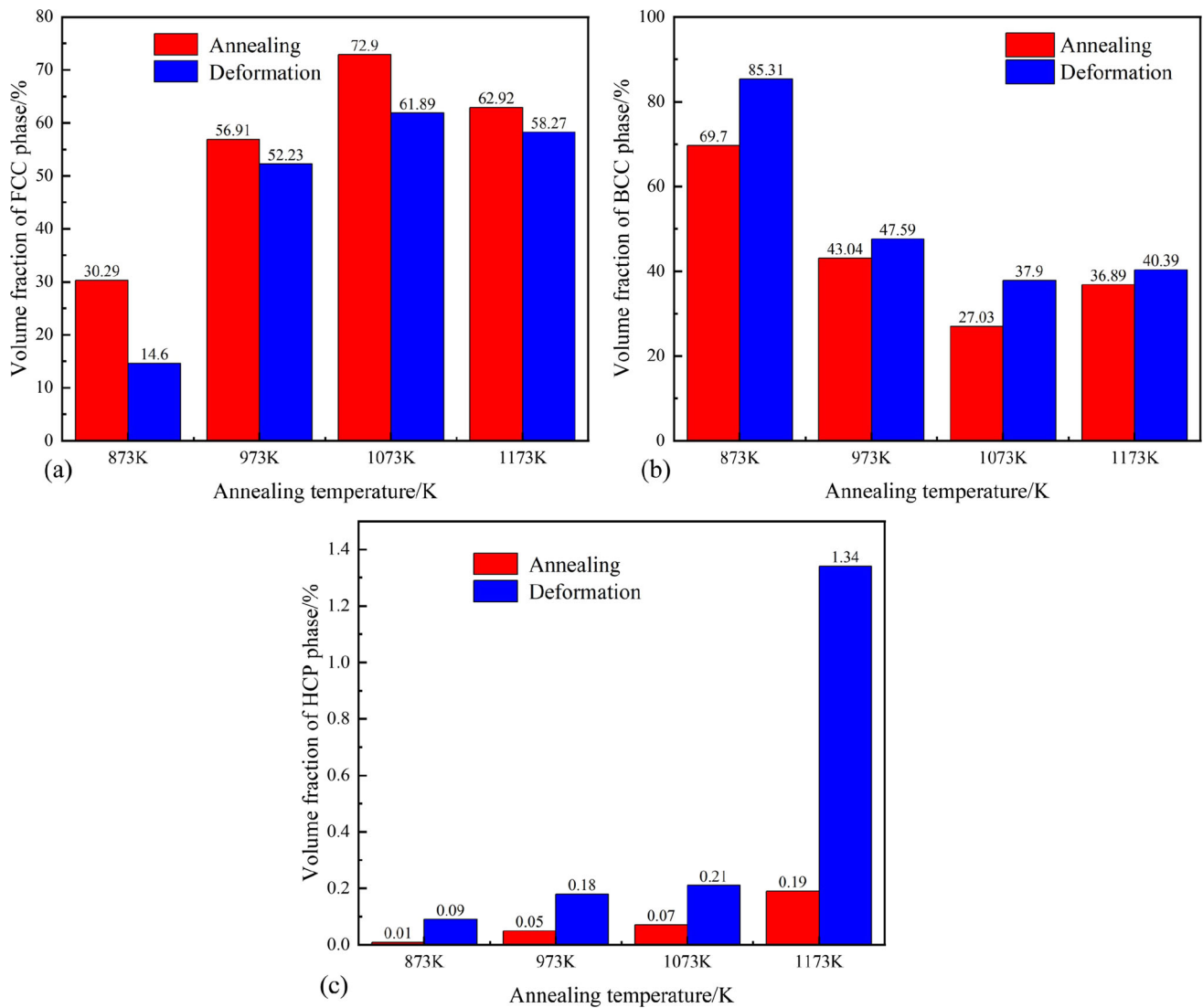
$$\theta = \frac{d\sigma}{d\varepsilon} \tag{Eq 1}$$

Here, σ and ε represent the true stress and strain, respectively.
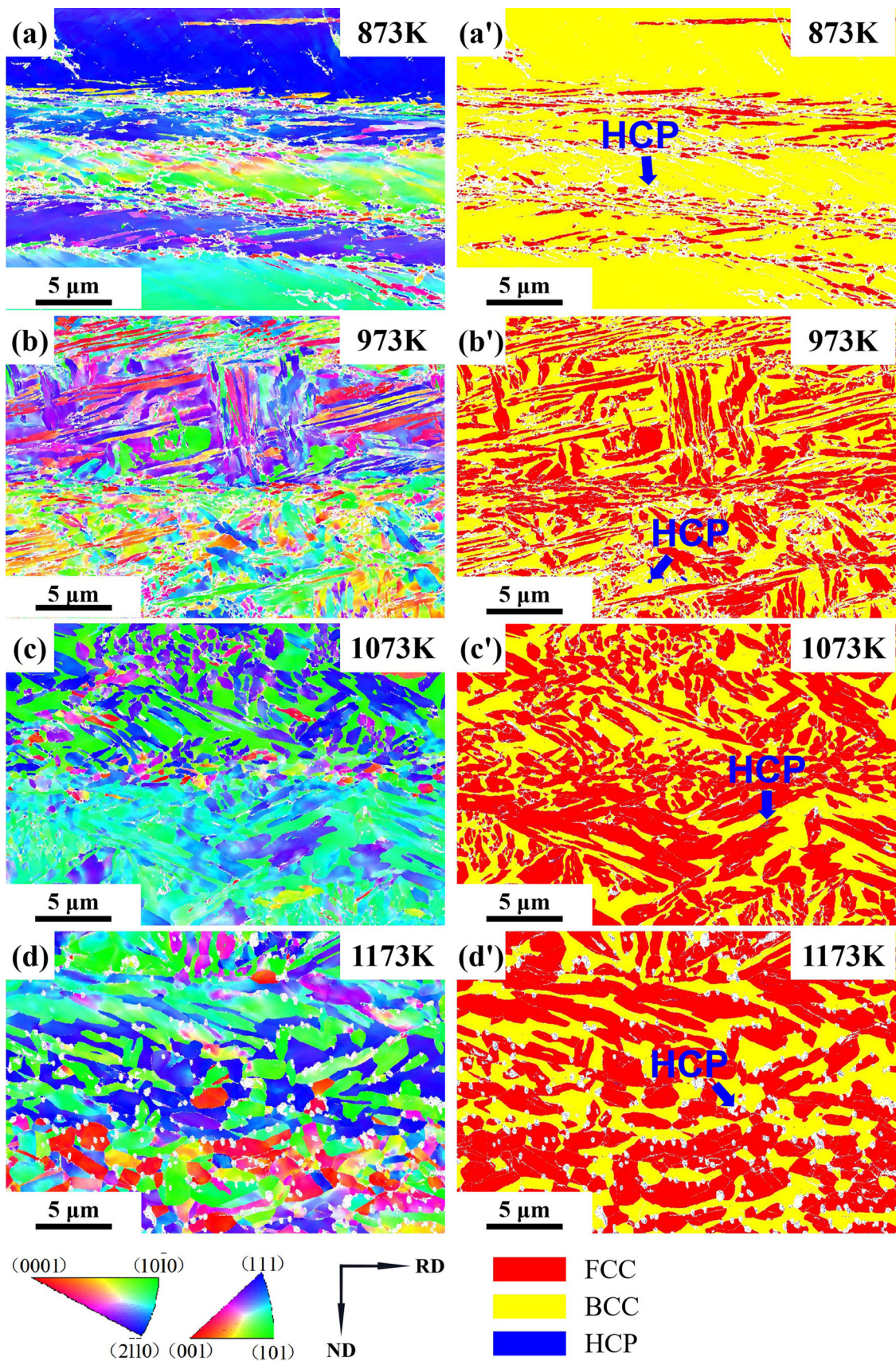
Fig. 8 EBSD images of samples annealed at different temperatures after tensile deformation: (a-d) IFP maps, (a′-d′) phase maps, (a, a′) 873 K-annealed, (b, b′) 973 K-annealed, (c, c′) 1073 K-annealed, (d, d′) 1173 K-annealed

Fig. 9 Volume fraction of the FCC phase, BCC phase and HCP phase of samples before and after tensile deformation: (a) FCC phase, (b) BCC phase, (c) HCP phase

Figure 10(b) shows the strain-hardening curve of the samples. After hot rolling, the sample exhibited two-stage strain-hardening behavior. Stage I showed a strong downward trend, which can be attributed to the direct transformation between elastic and plastic deformation. Stage II showed a slow downward trend until a fracture occurred. Both hot-rolled and 873 K annealed samples exhibited two-stage strain-hardening behavior, but the sample annealed at 873 K had higher strain-hardening rates in stage I. This may be due to the recovery of dislocations induced by rolling deformation after annealing, resulting in higher dislocation storage capacity. The samples annealed at 1073-1173 K exhibited three-stage strain-hardening behavior. Specifically, at stage I, its strain-hardening rate dropped rapidly. This stage was controlled by dislocation slip. At stage II, the strain-hardening rate rose briefly with increasing true strain; this stage is rare in HEAs but is common in some TWIP steels (Ref 32, 33). In this stage, the strain-hardening ability of the HEA was temporarily improved due to the combined influence of the TWIP and TRIP effects. However, due to the limited influence of the TWIP and TRIP effects, when the influence of the TWIP and TRIP effects reached

saturation, they immediately entered stage III. Compared with stage I, the strain-hardening rate in stage III also decreased, but the decreasing rate was slow. When the true strain approached the maximum value, the strain-hardening rate decreased rapidly until the alloy broke. It is shown in the literature that the increase in the strain-hardening rate in stage II is due to the transition from the bit slip mechanism to the twin deformation mechanism (Ref 34, 35). When deformation twins occur in plastic deformation, the dislocations are blocked by twin boundaries and the dislocations' average degrees of freedom decrease. The reduced average free path has the same influence as the dynamically reduced grain size, leading to an increase in the strain-hardening rate in stage II (dynamic Hall–Petch effect) (Ref 35-37).

As an essential parameter to evaluate the uniform plastic deformation of materials, the strain-hardening ability of materials is usually related to the ultimate tensile strength and fracture toughness (Ref 38). In the case of the uniaxial tensile test, the strain-hardening ability of materials can be defined as the ratio of the ultimate tensile strength to the yield strength of
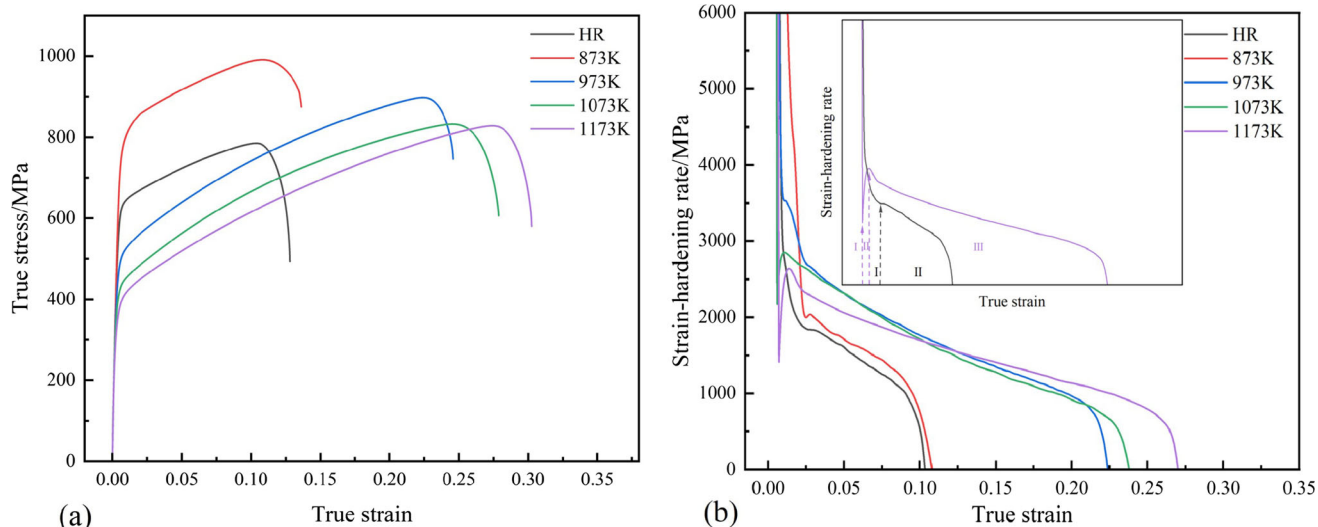
Fig. 10 True stress–strain curves and work hardening curves of hot-rolled and annealed samples: (a) true stress–strain curve, (b) strain-hardening curve

Table 2 Tensile properties and strain-hardening capacity (Hc) of the annealed HEA

Sample	$\sigma_{\text{true}}^{UTS}$, MPa	σ_{true}^{y}, MPa	H_C
HR	785.35	627.75	0.251
873 K	990.12	717.72	0.380
973 K	897.75	620.30	0.447
1073 K	832.36	537.79	0.548
1173 K	828.22	498.65	0.661

materials (Ref 39). In this study, the strain-hardening ability of samples can be calculated by the following formula:

$$H_C = (\sigma_{\text{true}}^{UTS} - \sigma_{\text{true}}^{y})/\sigma_{\text{true}}^{y} \quad \text{(Eq 2)}$$

Here, H_C represents the strain-hardening ability of the samples. The larger the H_C is, the stronger the ability to maintain uniform plastic deformation and the more delayed failure (Ref 39). The H_C values of the hot-rolled and annealed samples are listed in Table 2. The sample annealed at a higher temperature had a higher H_C value, which corresponded to a higher fracture strain.

4.2 Relationship Between Microstructure and Properties of HEA

The proportion of recrystallized grains increased with increasing annealing temperature. The size and distribution of recrystallized grains were also affected by the annealing temperature, which will impact the yield strength. Therefore, the effects of various strengthening mechanisms on the yield strength of the HEA were calculated to study the relationship between the microstructure and mechanical properties. The contribution of various strengthening mechanisms to the yield strength of the HEA can be described by the following equation (Ref 40):

$$\sigma_y = \sigma_0 + \sigma_{ss} + \sigma_{gb} + \sigma_{\rho} + \sigma_{p} \quad \text{(Eq 3)}$$

Here, σ_0 is the lattice friction stress, and σ_{ss}, σ_{gb}, σ_{ρ}, and σ_{p} are the strengthening contributions of the solid solute, grain boundary, dislocation, and precipitation, respectively. Because no precipitation was found in the annealed samples, σ_{p} can be ignored. The lattice friction σ_0 can be based on the yield strength of the homogeneous sample (Ref 24), which is assumed to be 125 MPa. Therefore, the formula for calculating the yield strength can be simplified as follows:

$$\sigma_y = \sigma_0 + \sigma_{SS} + \sigma_{gb} + \sigma_{\rho} \quad \text{(Eq 4)}$$

σ_{gb} is the contribution value of the grain boundary strengthening band, which can be described by the classical Hall–Petch relation (Ref 41, 42):

$$\sigma_{gb} = K_y \cdot d^{-1/2} \quad \text{(Eq 5)}$$

Here, d is the size of recrystallized grains, and K_y is the strengthening coefficient. For HEAs with complex structures, it cannot simply be assumed that the strength of the alloy comes from only one of them. To apply these effects readily to the present HEAs, several assumptions were employed. The contribution of the HCP phase with very little content in the annealed alloy is ignored. The BCC phase was regarded as having interfaces with the FCC phase only. Finally, formula (5) is corrected to obtain the following formula:

$$\sigma_{gb} = K_{FCC} \cdot d_{FCC}^{-\frac{1}{2}} \cdot V_{FCC} + K_{BCC} \cdot d_{BCC}^{-\frac{1}{2}} \cdot V_{BCC} \quad \text{(Eq 6)}$$

where K_{FCC} and K_{BCC} represent the strengthening coefficients of the FCC and BCC phases, respectively. V_{FCC} and V_{BCC} represent the volume fractions of the FCC and BCC phases, respectively. The values for K_{FCC} (490 MPa·$\mu m^{1/2}$) and K_{FCC} (61 MPa·$\mu m^{1/2}$) are derived from References (Ref 43) and (Ref 15), respectively. In this study, the phase fraction and grain size of the alloy after different annealing temperatures are different, and the volume fractions of the FCC phase and BCC phase after different annealing temperatures are obtained in Fig. 9. The grain size of the two phases in the alloy after annealing can be calculated. The grain sizes are shown in Table 3.

Table 3 Average grain size of the alloy after annealing

Annealing temperature, K	Regions	Average grain size, μm
873	FCC	0.45
	BCC	0.53
973	FCC	0.55
	BCC	0.58
1073	FCC	0.64
	BCC	0.59
1173	FCC	1.22
	BCC	0.99

Table 4 Dislocation density of samples annealed at different temperatures

Annealing temperature, K	Dislocation density, m^{-2}
873	2.6749×10^{14}
973	2.1222×10^{14}
1073	1.8156×10^{14}
1173	1.6699×10^{14}

To consider solution strengthening (Ref 44), Al is considered as a solute here. Therefore, the contribution of solution strengthening depended on the concentration of Al:

$$\sigma_{SS} = M \frac{G \cdot \varepsilon_S^{3/2} \cdot c^{1/2}}{700} \qquad (Eq\ 7)$$

Here, M denotes the Taylor factor for converting shear stress into normal stress (~ 3.06), and G denotes the shear modulus (~ 81 GPa (Ref 46)). The interaction parameter ε_s is defined as:

$$\varepsilon_S = \left| \frac{\varepsilon_G}{1 + 0.5\varepsilon_G} - 3\varepsilon_a \right| \qquad (Eq\ 8)$$

The interaction parameters, including modulus changes and atomic size mismatch, are defined as follows:

$$\varepsilon_G = \frac{1}{G} \frac{\partial G}{\partial c} \qquad (Eq\ 9)$$

$$\varepsilon_a = \frac{1}{a} \frac{\partial a}{\partial c} \qquad (Eq\ 10)$$

Here, a is the lattice constant of the solvent, which is 3.59 (Ref 17). In addition, considering that the change in ε_G is negligible compared with ε_a (Ref 45), the contribution value of solution strengthening can be easily calculated at various annealing temperatures.

Bailey Hirsch's formula (Ref 46) is used to describe this relationship:

$$\sigma_\rho = MaGb\rho^{1/2} \qquad (Eq\ 11)$$

Here, M is the Taylor factor (~ 3.06), α is a constant (~ 0.2 (Ref 47)), G is the shear modulus (~ 81 GPa), b is the Burgers vector, and ρ is the total dislocation density. ATEX software was used to calculate the total dislocation density of the specimens. The values are shown in Table 4.

Based on the above analysis, the contributions of solution strengthening, grain boundary strengthening, dislocation strengthening, and lattice friction force to yield strength can be calculated. The results are plotted in Fig. 11. The calculated results agreed with the experimental results, but there were still some differences. The following reasons may cause this difference: Some of the intrinsic parameters were taken from the CoCrFeNiMn (Ref 43) HEA or $Al_{0.5}CoCrFeMnNi$ (Ref 15) HEA in our calculations. In addition, the influence of the tiny phase transformation before yielding and the small HCP after annealing were neglected. In addition, considering the calculation error in the test and the instrument's measurement error, the calculated data's general trend was consistent with the experimental data. According to the calculation, the contribu-

tion of grain boundary strengthening and dislocation strengthening to the yield strength decreased gradually with increasing annealing temperature.

In this study, the HEA annealed at low temperatures had a high dislocation density. During tensile deformation, the movable dislocations began to slide and then were blocked at the boundaries of grains, subgrains, twins, or other obstacles, entangled with each other, and diffused rapidly. In this process, the rearrangement of the dislocation configuration led to dislocation unit formation, essentially a softening process. The formation of dislocation units would consume dislocations and release gradually accumulated strain energy to support further plastic deformation (Ref 24). Compared with the microstructure before the tensile test, the dislocation density in the alloy after the tensile test was much higher. The rapid diffusion of dislocations led to a considerable strain-hardening effect, which enabled the HEA to maintain high strength. With increasing annealing temperature, the dislocation density decreased, while recrystallized grains and annealing twins increased. Annealing twins were essential in providing stable strain hardening. In the subsequent tensile deformation, annealing twins can pin dislocations and promote dislocation diffusion, resulting in strain hardening (Ref 48). Due to incomplete recrystallization, a multiscale structure with a staggered distribution of deformed grains restored the subgrains, and recrystallized grains were formed. This results in an uneven distribution of the alloy grain size, further increasing the grain boundary-strengthening effect (Ref 49). In addition, during tensile deformation, the TRIP mechanism can change strength and ductility by delaying stress localization (necking) and driving uniform plastic deformation. Therefore, TRIP significantly increases strain hardening in the local stress zone (Ref 50). In this study, although the effect of TRIP was limited, the effect increased with increasing annealing temperature, which made the strain hardening continue to increase after annealing at a higher temperature.

5. Conclusion

In the present work, the effect of annealing after hot rolling on the microstructure evolution and tensile behavior of a tri-phase high-entropy alloy $(Fe_{50}Mn_{30}Co_{10}Cr_{10})_{91}Al_9$ (at.%) was investigated. The main findings of the present work can be summarized as follows:

1. Hot-rolled and annealed $(Fe_{50}Mn_{30}Co_{10}Cr_{10})_{91}Al_9$ (at.%) HEAs consisted of the FCC phase, BCC phase, and a small amount of HCP phase. After annealing at 873 K, there were many recovered subgrains, and the fraction of BCC phase and LAGBs was high. With increasing
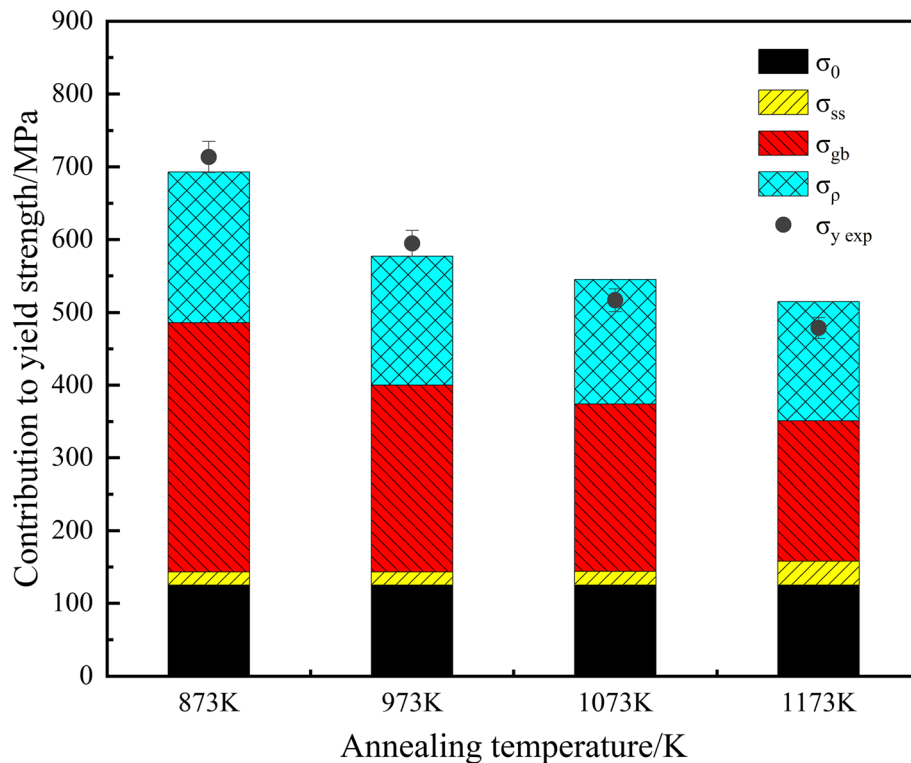
Fig. 11 Contribution of each strengthening mechanism to the YS of samples annealed at different temperatures

annealing temperature, the fraction of FCC phase increased and reached a maximum of 77.9%. The fraction of recrystallized grains and twin boundaries also increased.

2. Hot-rolled and annealed $(Fe_{50}Mn_{30}Co_{10}Cr_{10})_{91}Al_9$ (at.%) HEAs exhibited different mechanical properties. Compared with the hot-rolled HEA, the yield strength and tensile strength of the HEA annealed at 873 K increased by 14.5% and 25%, respectively, and there was no loss of ductility. Compared with the hot-rolled HEA, the ductility of the HEA annealed at 973 K-1073 K increased significantly.

3. Hot-rolled and annealed $(Fe_{50}Mn_{30}Co_{10}Cr_{10})_{91}Al_9$ (at.%) HEAs exhibited a multistage strain-hardening mechanism during plastic deformation, which was rarely seen in traditional HEAs. Moreover, a simple composite model was used to describe the relationship between the microstructure and mechanical properties of the annealed HEAs. This model offered a reasonable interpretation of the strengthening effect in the annealed HEAs.

References

1. J.W. Yeh, Alloy Design Strategies and Future Trends in High-Entropy Alloys, *JOM*, 2013, **65**(12), p 1759–1771.

2. Y.F. Ye, Q. Wang, J. Lu et al., High-Entropy Alloy: Challenges and Prospects, *Mater. Today*, 2016, **19**(6), p 349–362.

3. Y. Zhang, T.T. Zuo, Z. Tang et al., Microstructures and Properties of High-Entropy Alloys, *Prog. Mater. Sci.*, 2014, **61**, p 1–93.

4. B. Cantor, I.T.H. Chang, P. Knight et al., Microstructural Development in Equiatomic Multicomponent Alloys, *Mater. Sci. Eng. A*, 2004, **375–377**, p 213–218.

5. Z. Wang, S. Guo, and C.T. Liu, Phase Selection in High-Entropy Alloys: From Nonequilibrium to Equilibrium, *JOM*, 2014, **66**(10), p 1966–1972.

6. C.C. Juan, M.-H. Tsai, C.W. Tsai et al., Enhanced Mechanical Properties of HfMoTaTiZr and HfMoNbTaTiZr Refractory High-Entropy Alloys, *Intermetallics*, 2015, **62**, p 76–83.

7. Y.J. Zhao, J.W. Qiao, S.G. Ma et al., A Hexagonal Close-Packed High-Entropy Alloy: The Effect of Entropy, *Mater. Des.*, 2016, **96**, p 10–15.

8. Y. Zhang, X. Yang, and P.K. Liaw, Alloy Design and Properties Optimization of High-Entropy Alloys, *JOM*, 2012, **64**(7), p 830–838.

9. D.B. Miracle and O.N. Senkov, A Critical Review of High Entropy Alloys and Related Concepts, *Acta Mater.*, 2017, **122**, p 448–511.

10 I.S. Wani, G.D. Sathiaraj, M.Z. Ahmed et al., Evolution of Microstructure and Texture During Thermo-Mechanical Processing of a Two Phase Al_{0.5}CoCrFeMnNi High Entropy Alloy, *Mater. Charact.*, 2016, **18**, p 417–424.

11. J.Y. He, H. Wang, Y. Wu et al., High-Temperature Plastic Flow of a Precipitation-Hardened FeCoNiCr High Entropy Alloy, *Mater. Sci. Eng. A*, 2017, **686**, p 34–40.

12. S. Niu, H. Kou, T. Guo et al., Strengthening of Nanoprecipitations in an Annealed Al_{0.5}CoCrFeNi High Entropy Alloy, *Mater. Sci. Eng. A*, 2016, **671**, p 82–86.

13. J.Y. He, W.H. Liu, H. Wang et al., Effects of Al Addition on Structural Evolution and Tensile Properties of the FeCoNiCrMn High-Entropy Alloy System, *Acta Mater.*, 2014, **62**, p 105–113.

14. Z. Li, K.G. Pradeep, Y. Deng et al., Metastable High-Entropy Dual-Phase Alloys Overcome the Strength-Ductility Trade-Off, *Nature*, 2016, **534**(7606), p 227–230.

15. J.M. Park, J. Moon, J.W. Bae et al., Effect of Annealing Heat Treatment on Microstructural Evolution and Tensile Behavior of Al_{0.5}CoCrFeMnNi High-Entropy Alloy, *Mater. Sci. Eng. A*, 2018, **728**, p 251–258.

16. Q. Li, J.R. Cahoon and N.L. Richards, On the Calculation of Annealing Twin Density, *Scr. Mater.*, 2006, **55**(12), p 1155–1158.

17. P.P. Bhattacharjee, G.D. Sathiaraj, M. Zaid et al., Microstructure and Texture Evolution During Annealing of Equiatomic CoCrFeMnNi High-Entropy Alloy, *J. Alloys Compd.*, 2014, **587**, p 544–552.

18. B.R. Chen, A.C. Yeh, and J.W. Yeh, Effect of One-Step Recrystallization on the Grain Boundary Evolution of CoCrFeMnNi High Entropy Alloy and Its Subsystems, *Sci. Rep.*, 2016, **6**, p 22306.

19. G.S. Grewal and S. Ankem, Modeling Matrix Grain Growth in the Presence of Growing Second Phase Particles in Two Phase Alloys, *Acta Metall. Mater.*, 1990, **38**, p 1607–1617.

20. Z. Tang, M.C. Gao, H. Diao et al., Aluminum Alloying Effects on Lattice Types, Microstructures, and Mechanical Behavior of High-Entropy Alloys Systems, *JOM*, 2013, **65**(12), p 1848–1858.

21. J.C. Rao, H.Y. Diao, V. Ocelík et al., Secondary Phases in Al_xCoCrFeNi High-Entropy Alloys: An In-Situ TEM Heating Study and Thermodynamic Appraisal, *Acta Mater.*, 2017, **131**, p 206–220.

22. T. Lindner, M. Löbel, T. Mehner et al., The Phase Composition and Microstructure of Al_xCoCrFeNiTi Alloys for the Development of High-Entropy Alloy Systems, *Metals*, 2017, **7**, p 5.

23 C.L. Chen and M.J. Tan, Effect of Grain Boundary Character Distribution (GBCD) on the Cavitation Behavior During Superplastic Deformation of Al 7475, *Mater. Sci. Eng. A*, 2002, **338**, p 243–252.

24. J. Zhou, H. Liao, H. Chen, et al., Effects Of Hot-Forging and Subsequent Annealing on Microstructure and Mechanical Behaviors of $Fe_{35}Ni_{35}Cr_{20}Mn_{10}$ High-Entropy Alloy, *Mater. Charact.*, 2021, 178

25. X. He, L. Liu, T. Zeng, et al., Micromechanical Modeling of Work Hardening For Coupling Microstructure Evolution, Dynamic Recovery and Recrystallization: Application to High Entropy Alloys, *Int. J. Mech. Sci.*, 2020, 177

26. B. Bacroix, S. Queyreau, D. Chaubet et al., The Influence of the Cube Component on the Mechanical Behavior of Copper Polycrystalline Samples in Tension, *Acta Mater.*, 2018, **160**, p 121–136.

27. Y. Jin, B. Lin, M. Bernacki et al., Annealing Twin Development During Recrystallization and Grain Growth in Pure Nickel, *Mater. Sci. Eng. A*, 2014, **597**, p 295–303.

28 Q. Li, J.R. Cahoon, and N.L. Richards, Effects of Thermo-Mechanical Processing Parameters on the Special Boundary Configurations of Commercially Pure Nickel, *Mater. Sci. Eng. A*, 2009, **527**(1–2), p 263–271.

29. D. Ma, B. Grabowski, F. Körmann et al., Ab Initio Thermodynamics of the CoCrFeMnNi High Entropy Alloy: Importance of Entropy Contributions Beyond the Configurational One, *Acta Mater.*, 2015, **100**, p 90–97.

30. G.B. Olson and M. Cohen, Kinetics of Strain-Induced Martensitic Nucleation, *Metall. Trans. A*, 1975, **6**, p 791–795.

31. G.B. Olson and M. Cohen, A Perspective on Martensitic Nucleation, *Annu. Rev. Mater. Sci*, 1981, **11**(1), p 1–32.

32. S.W. Wu, G. Wang, J. Yi et al., Strong Grain-Size Effect on Deformation Twinning of an Al0.1CoCrFeNi High-Entropy Alloy, *Mater. Res. Lett.*, 2016, **5**(4), p 276–283.

33. G. Laplanche, A. Kostka, C. Reinhart et al., Reasons for the Superior Mechanical Properties of Medium-Entropy CrCoNi Compared to High-Entropy CrMnFeCoNi, *Acta Mater.*, 2017, **128**, p 292–303.

34. E.A. El-Danaf, S.R. Kalidindi and R.D. Doherty, Influence of Grain Size and Stacking-Fault Energy on Deformation Twinning in Fcc Metals, *Metall. Mater. Trans. A*, 1999, **30**, p 1223–1233.

35. N. Kumar, Q. Ying, X. Nie et al., High Strain-Rate Compressive Deformation Behavior of the $Al_{0.1}$CrCoNi High Entropy Alloy, *Mater. Des.*, 2015, **86**, p 598–602.

36. M.J. Jang, D.-H. Ahn, J. Moon et al., Constitutive Modeling of Deformation Behavior of High-Entropy Alloys with Face-Centered Cubic Crystal Structure, *Mater. Res. Lett.*, 2017, **5**(5), p 350–356.

37. B.C. De Cooman, Y. Estrin and S.K. Kim, Twinning-Induced Plasticity (TWIP) Steels, *Acta Mater.*, 2018, **142**, p 283–362.

38. X.H. Chen and L. Lu, Work Hardening of Ultrafine-Grained Copper with Nanoscale Twins, *Scr. Mater.*, 2007, **57**(2), p 133–136.

39. J. Luo, Z. Mei, W. Tian et al., Diminishing of Work Hardening in Electroformed Polycrystalline Copper with Nano-Sized and Uf-Sized Twins, *Mater. Sci. Eng. A*, 2006, **441**(1–2), p 282–290.

40. N. Kamikawa, K. Sato, G. Miyamoto et al., Stress–Strain Behavior of Ferrite and Bainite with Nano-Precipitation in Low Carbon Steels, *Acta Mater.*, 2015, **83**, p 383–396.

41 H. Shahmir, T. Mousavi, J. He et al., Microstructure and Properties of a CoCrFeNiMn High-Entropy Alloy Processed by Equal-Channel Angular Pressing, *Mater. Sci. Eng. A*, 2017, **705**, p 411–419.

42. S. Chen, K.K. Tseng, Y. Tong et al., Grain Growth and Hall–Petch Relationship in a Refractory HfNbTaZrTi High-Entropy Alloy, *J. Alloys Compd.*, 2019, **795**, p 19–26.

43. W.H. Liu, Y. Wu, J.Y. He et al., Grain Growth and the Hall–Petch Relationship in a High-Entropy FeCrNiCoMn Alloy, *Scr. Mater.*, 2013, **68**(7), p 526–529.

44. R.L. Fleischer, Substitutional Solution Hardening, *Acta Metall.*, 1963, **11**, p 203–209.

45. J.Y. He, H. Wang, H.L. Huang et al., A Precipitation-Hardened High-Entropy Alloy with Outstanding Tensile Properties, *Acta Mater.*, 2016, **102**, p 187–196.

46. J.E. Bailey and P.B. Hirsch, The Dislocation Distribution, Flow Stress, and Stored Energy in Cold-Worked Polycrystalline Silver, *Philos. Mag.*, 1960, **5**(53), p 485–497.

47. J.Y. He, C. Zhu, D.Q. Zhou et al., Steady State Flow of the FeCoNiCrMn High Entropy Alloy at Elevated Temperatures, *Intermetallics*, 2014, **55**, p 9–14.

48 Y. Xin, L. Lv, H. Chen et al., Effect of Dislocation-Twin Boundary Interaction on Deformation by Twin Boundary Migration, *Mater. Sci. Eng. A*, 2016, **662**, p 95–99.

49. S.W. Wu, G. Wang, Q. Wang et al., Enhancement of Strength-Ductility Trade-Off in a High-Entropy Alloy Through a Heterogeneous Structure, *Acta Mater.*, 2019, **165**, p 444–458.

50. Z. Li, C.C. Tasan, K.G. Pradeep et al., A TRIP-Assisted Dual-Phase High-Entropy Alloy: Grain Size and Phase Fraction Effects on Deformation Behavior, *Acta Mater.*, 2017, **131**, p 323–335.